OPEN

Physical electro-thermal model of resistive switching in bi-layered resistance-change memory

Sungho Kim, Sae-Jin Kim, Kyung Min Kim, Seung Ryul Lee, Man Chang, Eunju Cho, Young-Bae Kim, Chang Jung Kim, U. -In Chung & In-Kyeong Yoo

Samsung Advanced Institute of Technology, Nongseo-dong, Giheung-gu, Yongin-si, Gyeonggi-do 446-712, Korea.

Tantalum-oxide-based bi-layered resistance-change memories (RRAMs) have recently improved greatly with regard to their memory performances. The formation and rupture of conductive filaments is generally known to be the mechanism that underlies resistive switching. The nature of the filament has been studied intensively and several phenomenological models have consistently predicted the resistance-change behavior. However, a physics-based model that describes a complete bi-layered RRAM structure has not yet been demonstrated. Here, a complete electro-thermal resistive switching model based on the finite element method is proposed. The migration of oxygen vacancies is simulated by the local temperature and electric field derived from carrier continuity and heat equations fully coupled in a 3-D geometry, which considers a complete bi-layered structure that includes the top and bottom electrodes. The proposed model accurately accounts for the set/reset characteristics, which provides an in-depth understanding of the nature of resistive switching.

O xide-based resistance-change memories (RRAMs) have been studied intensively during the past decade and have attracted increasing interest as potential next-generation nonvolatile memories[1]. To explain their resistive switching behaviors, researchers have proposed various mechanisms, among which the concept of formation/rupture of conductive filaments (CFs) has been widely accepted[2]. The transition from a high-resistance state (HRS) to a low-resistance state (LRS) is called the set process, which is interpreted as a defect-induced soft breakdown associated with the migration of non-lattice oxygen ions toward the electrode[3]. In contrast, the transition from the LRS to the HRS is called the reset process, in which electric-field-enhanced oxygen ion-hopping ruptures the CFs[4]. In the case of bipolar resistive switching, the voltages for the set and reset processes have the opposite polarities, thus revealing the role of voltage-driven migration of oxygen ions[5–8]. Moreover, recent studies have pointed out the crucial role of temperature in the voltage-driven migration process at the moment of set or reset transition[9,10].

On the basis of comprehensive and intensive studies, the nature of the filament during the set and reset processes is now comprehensible. The presence of one or more localized CFs has also been confirmed by direct microscopic methods[11,12] and indirect electrical measurements. In addition, several phenomenological or physical models have predicted the consistent resistance-change behavior (i.e., current-voltage (I–V) characteristics) of RRAMs[5,8,9]. However, existing models have apparently overlooked an important fact. As mentioned earlier, the thermal effect is an essential factor of oxygen ion migration during the set and reset processes. Therefore, to predict the temperature inside the CF accurately, the thermal properties of both the electrodes and the oxide layer should be included in a model. However, most previous models have ignored the effect of electrodes and assumed either the CF/electrode interface to be at room temperature[5,9] or the temperature inside the CF to be constant[13,14]. Although Menzel *et al.* have recently proposed an advanced electro-thermal model that considers both the top and the bottom electrodes to calculate the temperature of the CF precisely[10], a physical model that predicts the I–V characteristics of an RRAM accurately in a complete bi-layered RRAM structure has not yet been demonstrated.

In this work, a numerical model, which is based on temperature- and field-accelerated migration of oxygen vacancies, is presented for bipolar RRAMs. A 2-D axis-symmetric finite element simulation model, which allows a quantitative analysis of field and temperature contributions, accounts accurately for the set/reset characteristics of both the DC and the AC responses. The proposed model also provides a microscopic interpretation of inter-mediate set/reset states based on differences in the CF morphology.
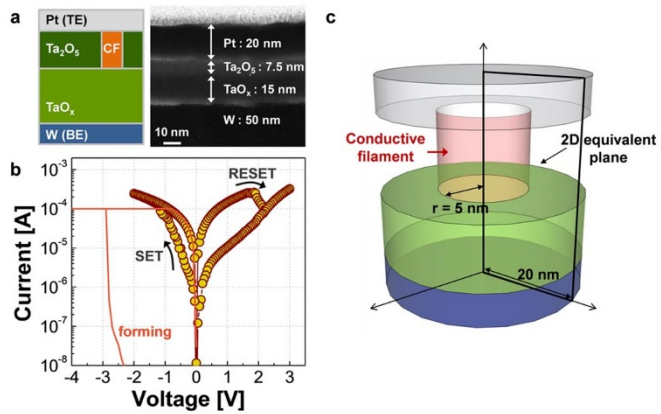
Figure 1 | Schematic diagram and simulated geometry. (a) Schematic and cross-sectional TEM images of the Pt/Ta$_2$O$_5$/TaO$_x$/W bi-layered RRAM device. (b) Typical I–V characteristic of Pt/Ta$_2$O$_5$/TaO$_x$/W device. (c) Simulated geometry used in calculation. The axisymmetric geometry reduces the problem from one of three dimensions to one of two dimensions.

Results

The tantalum-oxide-based bi-layered RRAM consisted of a high resistive Ta$_2$O$_5$ layer on top of a less resistive TaO$_x$ layer (see Methods for details), which was sandwiched by a top electrode (TE) of Pt and a bottom electrode (BE) of W, as shown in Fig. 1(a). When a large negative voltage is applied to the pristine device (a process called "forming" shown in Fig. 1(b)), positively charged oxygen vacancies are attracted from the TaO$_x$ layer to the TE, forming a CF[15,16]. This CF is described as a doped region where oxygen vacancies (V$_o$) act as dopants and thus contribute to local electrical and thermal conductivity values[17]. The simulation, which is started immediately after the forming process, features a continuous CF that connects the top and bottom electrodes (Fig. 1(c)). After the forming process, the set and reset processes are described through V$_o$ migration induced by the local electric field and temperature due to Joule heating[5,17]. Thus, simulation of the set/reset transitions requires the self-consistent solution of three partial differential equations (PDEs): (1) a drift/diffusion continuity equation for V$_o$ transport, (2) a current continuity equation for electrical conduction, and (3) a Fourier equation for Joule heating, as shown in Fig. 2.
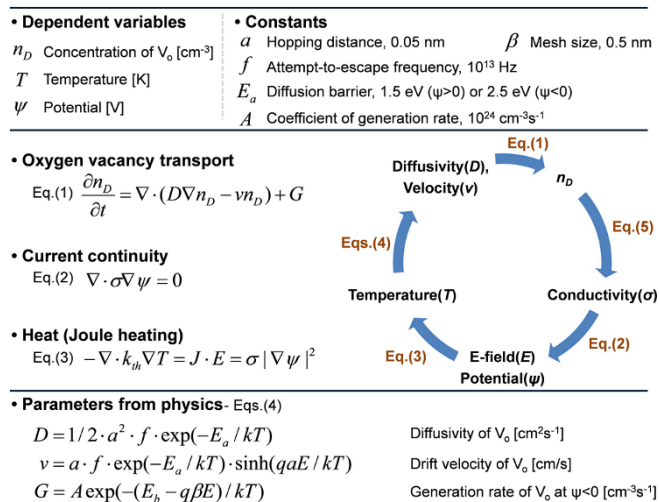

Figure 2 | The equations and parameters in the proposed model. Three PDEs are self-consistently solved within a numerical solver.
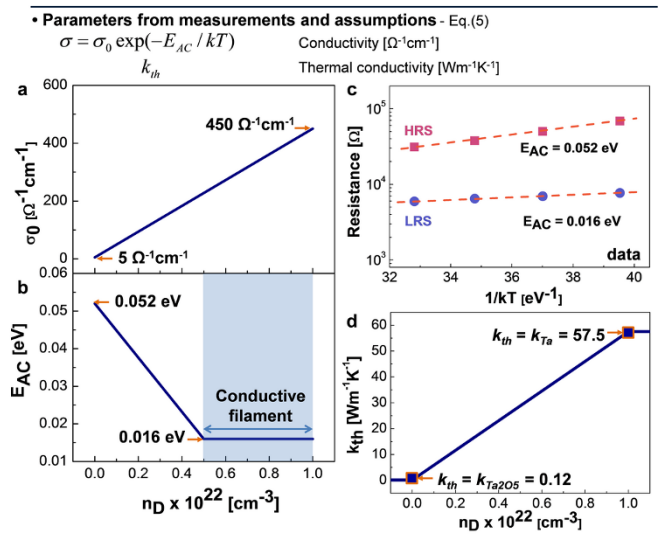

Figure 3 | Parameters from measurements and assumptions. (a) Electrical conductivity pre-exponential factor σ_0, (b) assumed activation energy for conduction E_{AC}, (c) measured E_{AC} at both HRS and LRS, and (c) assumed thermal conductivity k_{th} as a function of local V$_o$ density n_D.

To describe the drift/diffusion of V$_o$ migration, a simple 1D rigid point ion model by Mott and Gurney is employed[18]. Although the ion-hopping model by Mott and Gurney is applicable oxygen ions rather than oxygen vacancies, here, we believe that both oxygen vacancies and ions can be described by the same equations except for the detailed physical parameters. Diffusion is given by $D = 1/2\,a^2 f\exp(-E_a/kT)$, and the drift velocity is given by $v = a\,f\exp(-E_a/kT)\sinh(qaE/kT)$, where f is the attempt-to-escape frequency (10^{13} Hz)[18], a is the effective hopping distance (0.05 nm), and E_a is the activation energy of migration. In fact, the effective hopping distance (a) has a range of a few nanometers ($\sim$1 nm)[18]. However, the value of 0.05 nm was used in this work for the purpose of best fitting the experimental data. This inconsistency is presumably due to differences in the physical nature of oxygen vacancies and oxygen ions. Considering the drift and diffusion, the time-dependent evolution of V$_o$ concentration (n_D) can be expressed by the continuity equation, as follows:
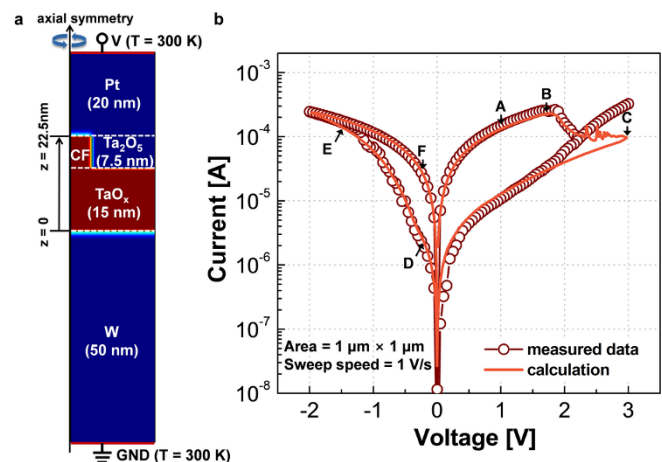

Figure 4 | Simulated boundary conditions and calculated results. (a) Cross section of the simulated cell. A uniform doping concentration of $n_D = 1 \times 10^{22}$ cm^{-3} was defined within the CF and TaO$_x$ layer as the initial forming state. (b) Measured and calculated I–V characteristics.
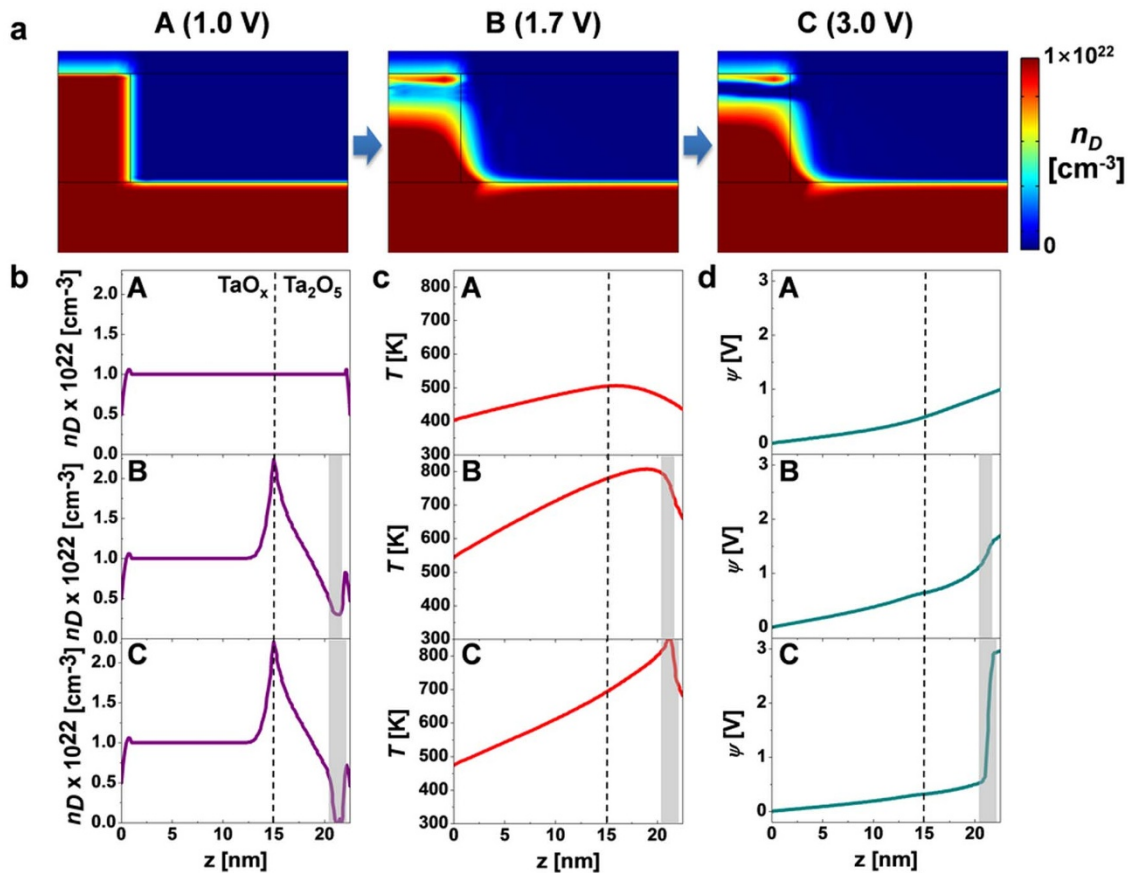
Figure 5 | Simulation results for the reset transition. (a) Calculated map of V_o density (n_D). Calculated profiles of (b) n_D, (c) T, and (d) ψ for states A (1.0 V), B (1.7 V), and C (3.0 V) as depicted in Fig. 4(b). The position of z = 15 nm indicates the Ta_2O_5/TaO_x interface. The depleted gap, defined for $n_D < 5 \times 10^{21}$ cm^{-3}, is marked by the shaded area.

$$\frac{\partial n_D}{\partial t} = \nabla \cdot (D \nabla n_D - v n_D) + G. \tag{1}$$

Here, G is the generation term to describe the set process. The kinetics of the set process can be interpreted as a dielectric soft breakdown associated with the migration or generation of V_o through thermally activated hopping. The CF growth rate is assumed to be proportional to the ion migration rate, which is given by $G = A \exp(-(E_b - qV)/kT) = A \exp(-(E_b - q\beta E)/kT)$[19,20], where A is a pre-exponential constant, E_b is the energy barrier for ion hopping (1 eV), and β is the mesh size in the simulation (0.5 nm). Term $q\beta E$ describes the lowering of the barrier attributed to the applied field. This lowering forces the V_o to move along the direction of the electric field. To express the set process that occurs only at a negative bias, the generation term is also applied exclusively at a negative bias. Equation (1) can be solved with the current continuity equation for electrical conduction, as follows:

$$\nabla \cdot \sigma \nabla \psi = 0 \tag{2}$$

where σ is the electrical conductivity, and with the steady-state Fourier equation for Joule heating

$$-\nabla \cdot k_{th} \nabla T = J \cdot E = \sigma |\nabla \psi|^2 \tag{3}$$

where k_{th} is the thermal conductivity. The transient contribution to the Fourier equation was disregarded, given the relatively fast thermal response of approximately 1 ps (see Supplementary Information)[5,9].

The three PDEs in equations (1)–(3) are self-consistently solved by a numerical solver (COMSOL) to calculate n_D, ψ (potential), and T (temperature). To solve equation (3), models for electrical conductivity (σ) and thermal conductivity (k_{th}) in the oxide and in the CF are required. To this end, both the electrical and the thermal conductivities are assumed to depend on n_D, as shown in Fig. 3[5,9]. The electrical conductivity is given by the Arrhenius equation[21], $\sigma = \sigma_0 \exp(-E_{AC}/kT)$, where σ_0 is a pre-exponential factor and E_{AC} is the activation energy for conduction. As shown in Figure 3(a), σ_0 is assumed to linearly increase from 5 to 450 Ω^{-1}cm^{-1} with an increase in n_D; these values correspond to the measured values of resistivity at both the LRS and the HRS, respectively. In addition, Figure 3(b) shows the conduction activation energy E_{AC} used in the calculations. The activation energy is 0.016 eV for high n_D and linearly increases to 0.052 eV with a decrease in n_D, consistent with the measured data shown in Figure 3(c). Moreover, a linear dependence of k_{th} on n_D is assumed on the basis of the Wiedemann-Franz law, as shown in Figure 3(d)[5]. The minimum value for $n_D = 0$ refers to the thermal conductivity of the insulating Ta_2O_5, $k_{Ta2O5} = 0.12$ Wm^{-1}K^{-1} for T = 300 K[22]. The maximum k_{th} value at high n_D corresponds to that of the metallic CF, i.e., thermal conductivity of tantalum $k_{Ta} = 57.5$ Wm^{-1}K^{-1}. Here, a maximum V_o density of 1×10^{22} cm^{-3} is chosen approximately where it corresponds to a relative atomic concentration of 20%. Although the particular choice of the maximum V_o value and the linear approximations of σ_0, E_{AC}, and k_{th} appear to have a weak physical background, the calculation results based on these assumptions show good consistency with the experimental data; therefore, these assumptions do not limit the validity of the calculations.

Figure 4(a) shows the simulated region of the tantalum-oxide-based bi-layered RRAM. In the actual calculations, the axisymmetric geometry allowed the 3-D problem to be reduced to a 2-D solution with a radial coordinate and a vertical coordinate. The active oxide
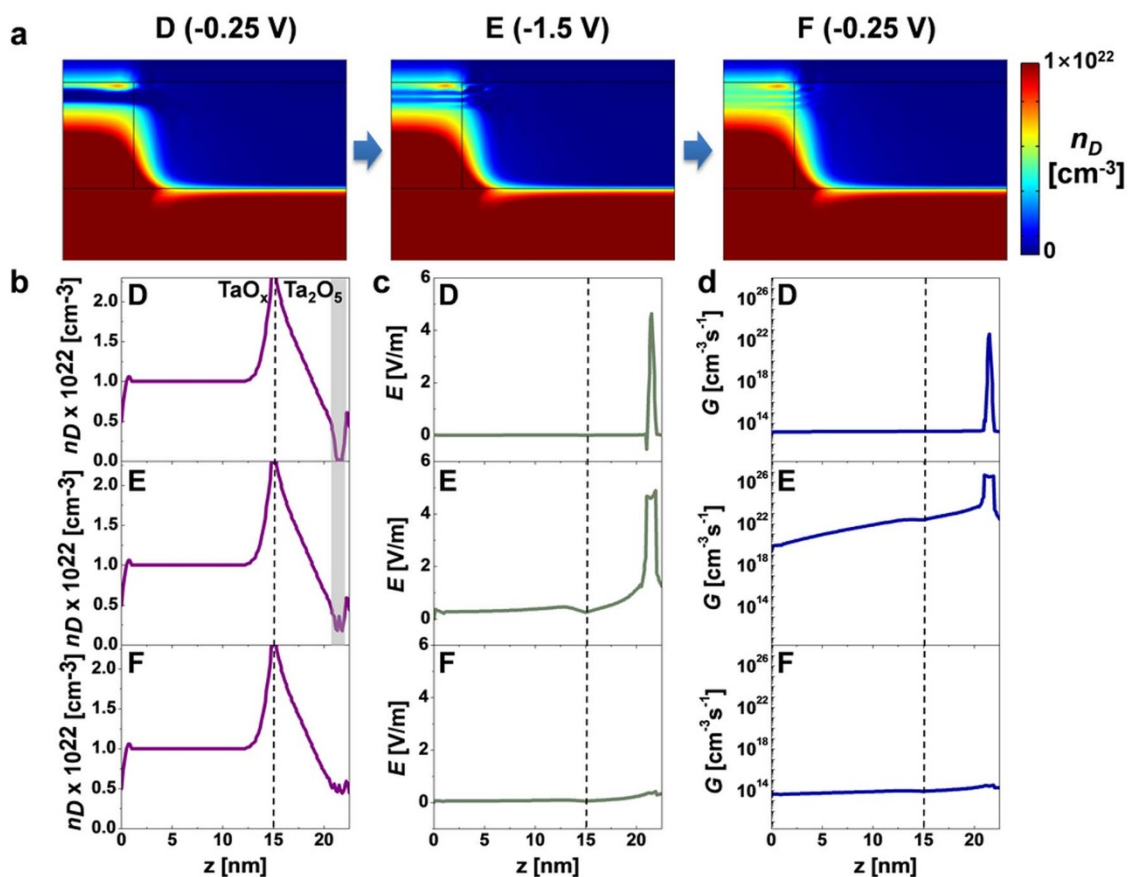
Figure 6 | Simulation results for the set transition. (a) Calculated map of V$_o$ density (n_D). Calculated profiles of (b) n_D, (c) E, and (d) G for states D (-0.25 V), E (-1.5 V), and F (-0.25 V), as depicted in Fig. 4(b).

materials (Ta$_2$O$_5$ and TaO$_x$ layers) are contacted by two electrodes, and all layers including the two electrodes are considered in the calculations (Pt TE, $\sigma_{Pt} = 10^5$ Ω^{-1}cm^{-1}, $k_{Pt} = 71.6$ Wm^{-1}K^{-1}; W BE, $\sigma_W = 2 \times 10^5$ Ω^{-1}cm^{-1}, $k_W = 173$ Wm^{-1}K^{-1}). The boundary conditions for equation (2) are $\psi = 0$ and $\psi = V$ at the bottom and top electrodes, respectively. The outermost boundaries of the two electrodes are defined as ideal heat sinks with boundary conditions T = 300 K; this simplifying assumption is reasonable because the electrode area is generally large with respect to the CF. For V$_o$ drift/diffusion, no V$_o$ flux was assumed at the TE/Ta$_2$O$_5$ and TaO$_x$/BE interfaces. In addition, only diffusion was considered in the TaO$_x$ layer (i.e., the drift term (v) of equation (1) is zero) because this layer only serves the role of an oxygen vacancy reservoir[15,16]. A uniform doping concentration of $n_D = 1 \times 10^{22}$ cm^{-3} was defined within the CF and TaO$_x$ layer as the initial state (i.e., the forming state). The CF size was set to a diameter of 10 nm, in agreement with direct evaluations by using conductive atomic force microscopy[23].

Discussion

Figure 4(b) shows the measured and calculated I–V characteristics during the set and reset processes after the forming process. The reset transition starts at 1.85 V and the resistance gradually increases, finally achieving a difference of roughly one decade after V$_{RESET}$ = 3.0 V. Similarly, the set transition starting at -0.5 V also shows good consistency with the measured data. Figure 5 shows calculated (a) 2-D maps of n_D as well as 1-D profiles of (b) n_D, (c) T, and (d) ψ at bias points A, B, and C. As the voltage increases during the reset sweep, the temperature increases as a consequence of Joule heating, as shown in Fig. 5(c). V$_o$ migration is localized at the point of maximum temperature (i.e., near the TE) owing to the activation of drift

velocity by exponential T. Consequently, V$_o$ migrates toward the BE, resulting in the opening of a depleted gap. The opposite process occurs in the set transition. Figure 6 shows the calculated (a) 2-D maps of n_D and the 1-D profiles of (b) n_D, (c) E (electric field), and (d) G (generation rate of V$_o$) at the bias points D, E, and F. Given that the electric field at the depleted gap increases with an increase in the negative bias, the generation rate of V$_o$ increases, as shown in Figs. 6(c) and 6(d). Consequently, the depleted gap at the CF is refilled by V$_o$, after which the high electric field is no longer applied to
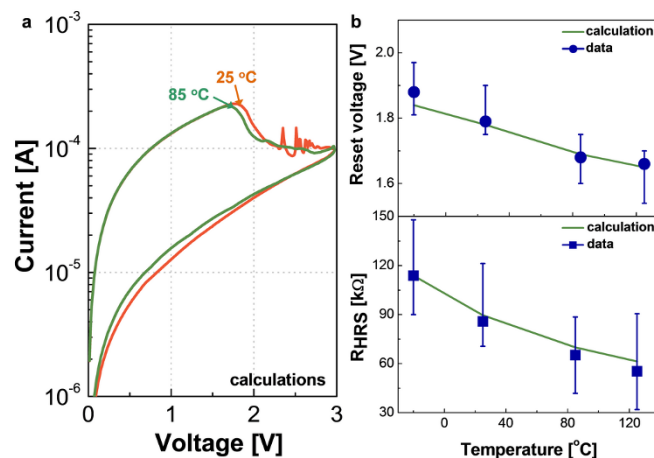

Figure 7 | Temperature dependency. (a) Calculated I–V characteristics at different device temperatures. Measured and calculated data for the (b) reset transition voltage and (c) resistance value of HRS.
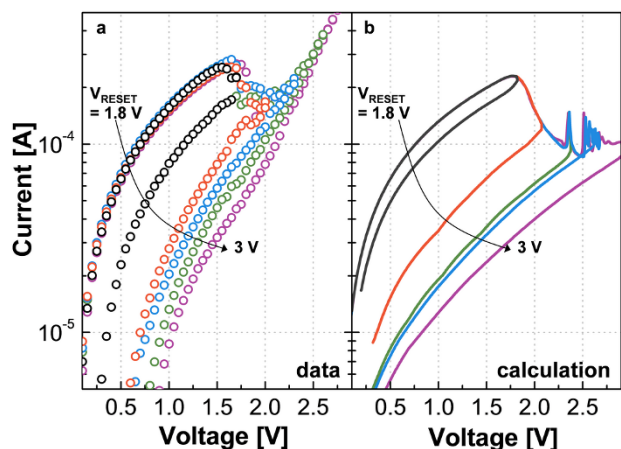
4

Figure 8 | Gradual reset process. (a) Measured and (b) calculated *I–V* curves, showing reset transition, obtained by varying V$_{RESET}$ (1.8 V to 3 V).

the CF. This suppresses further V$_o$ generation or migration and is responsible for a self-limiting set transition.

By applying different boundary conditions of temperature, the thermal effect on the *I–V* characteristics can be predicted by calculations. Figure 7(a) shows the calculated *I–V* curves under different temperature conditions. The reset transition voltage (i.e., the moment at which the resistance starts to decrease) noticeably decreases with an increase in the device temperature. In addition, the resistance at the HRS increases with an increase in the device temperature. The reset transition occurs at a lower bias voltage because V$_o$ migration (drift and diffusion) is more favorable at higher device temperatures. Moreover, the difference of conduction curve at the HRS is due to the temperature-dependent conductivity enhancement of σ through the Arrhenius equation. These two distinctive features agree well with the experimental data shown in Figs. 7(b) and 7(c), where the measurements are carried out in the range of −20°C–85°C; accordingly, the simulation accurately reflects the thermal effect for the set and reset transitions. To further verify the simulated results, Figures 8(a) and 8(b) show the measured and calculated *I–V* curves, including reset sweeps stopped at various values of V$_{RESET}$. The simulation accurately reproduces the different features of resistive switching with different values of V$_{RESET}$ and predicts a gradual reset transition behavior.
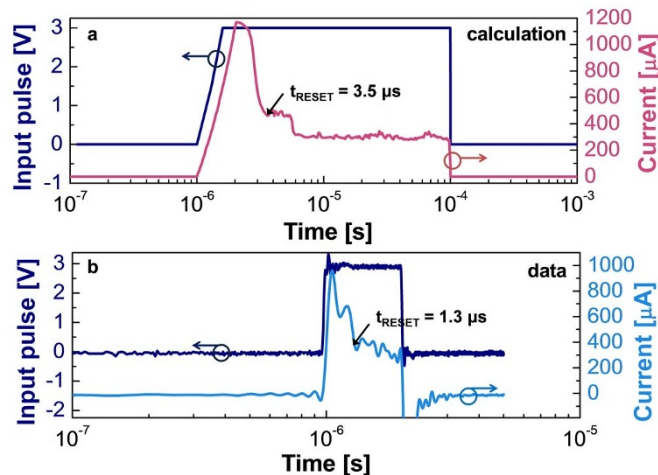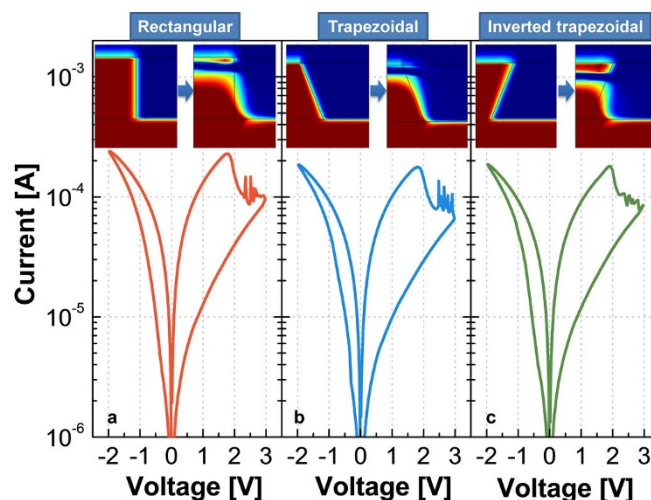

Figure 10 | Calculated *I–V* curves for filaments of different shapes. (a) rectangular, (b) trapezoidal, and (c) inverted trapezoidal. Despite the different shapes, the position of the depleted gap is almost identical. In addition, the *I–V* characteristics are also independent of the filament shape.

The application of the proposed model is not limited to reproducing the DC *I–V* characteristics. Time-dependent reset characteristics were further explored by investigating the response to square pulses. Time-resolved experiments were carried out in which a series of set/reset pulses was applied to the RRAM device with a serially connected resistor, and the response to an AC pulse was simultaneously detected by an oscilloscope. Figures 9(a) and 9(b) show the calculated and measured response profiles to the applied reset pulse as a function of time. When a single square pulse for the reset transition is applied to the device, the response current increases following a voltage increment because the initial state of the device is in the LRS. Over time, the response current rapidly decreases, which indicates the moment of reset transition. The measured time to the reset transition (t_{RESET}) is 1.3 µs for the input pulse shown in Fig. 9(b), which is comparable to the calculated value of t_{RESET} = 3.5 µs. Consequently, the simulation can describe the AC resistance-change response reliably in addition to the DC *I–V* characteristics.

Although the morphology of the CF has been observed by direct imaging with transmission electron microscopy (TEM), the effort required was extensive and the extracted results were insufficiently informative for comprehensively understanding the mechanism of
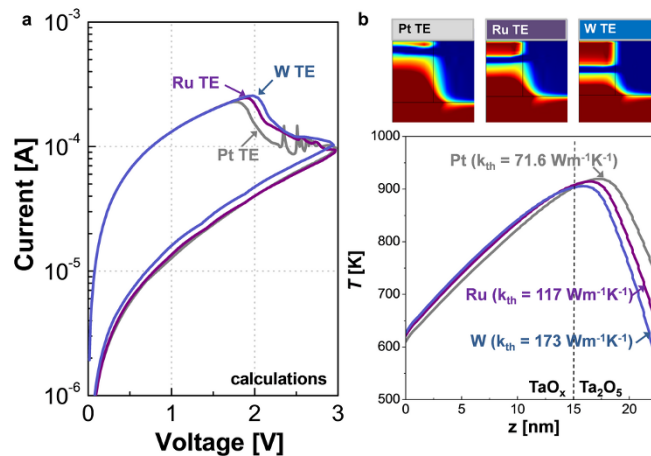

Figure 9 | Transient response. (a) Measured and (b) calculated AC response as a function of time.

Figure 11 | Effect of different TE materials. (a) Calculated *I–V* curves for different TE materials. (b) 2-D maps of n_D corresponding to TE materials, and temperature profiles in the CF and TaO$_x$ layer.

resistive switching[11]. In contrast, a merit of the simulation is that it provides a microscopic interpretation of intermediate set/reset states based on differences in the CF morphology. As mentioned above, the thermal properties of both the electrodes and the oxide layer should be included in the model to accurately describe the resistive switching phenomenon. Previously reported models predicted that the depleted gap at the reset transition should be positioned in the middle of the CF when temperature-driven process is dominant[4,9,17]. On the other hand, several papers have verified by electrical measurements that the depleted gap is located near the electrode/oxide interface. To overcome this disagreement between the model and the measurement result, modified models have been explained that the depleted gap can be located near the electrode/oxide interface, particularly when the shape of the CF is conical[24,25]. However, the analyses based on these modified pre-existing models are also inaccurate because they did not consider the thermal property of the electrodes. Figure 10 shows the $I-V$ characteristics and 2-D maps of n_D corresponding to filaments differing in their initial shape: (a) rectangular, (b) trapezoidal, or (c) inverted trapezoidal. It should be noted that the location of the depleted gap in the CF is independent of the shape. In particular, the filament with an inverted trapezoidal shape changes to a rectangular one after consecutive switching cycles. These results imply either that the depleted gap is not always located in the middle of the CF or that its location depends on the shape of the filament. Indeed, a crucial factor for the reset transition is the thermal conductivity ratio between the TE and the oxide. Figure 11(a) shows the calculated $I-V$ characteristics based on different TE materials, and Figure 11(b) shows the corresponding 2-D maps of n_D and the temperature profiles. The position of the depleted gap in the CF is determined by the thermal conductivity of the TE, and the DC $I-V$ characteristics are also distinct. (The BE material has a negligible effect owing to the presence of a relatively thick TaO$_x$ layer. In the case of a single-layered RRAM, the effect of the BE is also significant). As the thermal conductivity of the TE increases, the generated heat by Joule heating is confined within the oxide layer; consequently, the depletion gap of the CF is positioned away from the TE/oxide interface. Therefore, the effect of the electrodes should be considered in an analytical model to predict the nature of resistive switching accurately. The model proposed here provides an accurate interpretation of intermediate set/reset states based on differences in the CF morphology.

In summary, a physical and numerical model has been proposed on the basis of temperature/field-driven migration of oxygen vacancies in bi-layered bipolar RRAM devices. The proposed model allows the calculation of resistance-change characteristics for both the DC and the AC input signals. By considering the top and bottom electrodes, a more accurate temperature profile than that of the pre-existing models is obtained, which in turn leads to more accurate simulation results. The proposed model is potentially useful for gaining physical insights into the morphology of the CF during set and reset transitions, which is valuable for exploring the scaling and multilevel capabilities of RRAM devices.

Methods

All measured samples (Pt/Ta$_2$O$_5$/TaO$_x$/W devices) had a 1 μm × 1 μm crossbar structure. A 50-nm-thick W layer was deposited by sputtering and then patterned by dry etching to form the bottom electrode (BE) on a 3-nm-thick adhesion Ti/500-nm-thick SiO$_2$/Si substrate. Then, a 20-nm-thick conducting TaOx layer was deposited on the BE by DC magnetron sputtering in a reactive O$_2$ + Ar ambient, with Ta as the target. Subsequently, an insulating Ta$_2$O$_5$ layer was formed by a pulsed O$_2$ plasma oxidation process that involved a 2-s plasma-on step and a 4-s plasma-off (purge) step in a single cycle. The total oxidation time was controlled by the number of cycles, which was 80 in the present study. Finally, a 20-nm-thick Pt layer was evaporated and patterned by a lift-off process.

The DC electrical characterizations were carried out by an Agilent B1500A semiconductor analyzer in the voltage-sweep mode. During AC pulse measurements, a series resistor (1 kΩ) was serially connected to the RRAM device. Input pulses were generated by a B1500A, and the response was detected by an oscilloscope (Tektronix DPO 70604).

1. Yang, J. J., Strukov, D. B. & Stewart, D. R. Memristive devices for computing. *Nat. Nanotechnol.* **8**, 13–24 (2013).
2. Waser, R., Dittmann, R., Staikov, G. & Szot, K. Redox-based resistive switching memories-Nanoionic mechanisms, prospects, and challenges. *Adv. Mater.* **21**, 2632–2663 (2009).
3. Xu, N. *et al.* Characteristics and mechanism of conduction/set process in TiN/ZnO/Pt resistance switching random-access memories. *Appl. Phys. Lett.* **92**, 232112 (2008).
4. Yu, S. & Wong, H.-S. P. A phenomenological model for the reset mechanism of metal oxide RRAM. *IEEE Electron Device Lett.* **31**, 1455–1457 (2010).
5. Larentis, S., Nardi, F., Balatti, S., Gilmer, D. C. & Ielmini, D. Resistive switching by voltage-driven ion migration in bipolar RRAM – Part II: Modeling. *IEEE Trans. Electron Devices* **59**, 2468–2475 (2012).
6. Janousch, M. *et al.* Role of oxygen vacancies in Cr-doped SrTiO$_3$ for resistance-change memory. *Adv. Mater.* **19**, 2232–2235 (2007).
7. Nardi, F., Larentis, S., Balatti, S., Gilmer, D. C. & Ielmini, D. Resistive switching by voltage-driven ion migration in bipolar RRAM – Part I: Experimental study. *IEEE Trans. Electron Devices* **59**, 2461–2467 (2012).
8. Yu, S., Guan, X. & Wong, H.-S. P. On the stochastic nature of resistive switching in metal oxide RRAM: Physical modeling, Monte Carlo simulation, and experimental characterization. *IEDM Tech. Dig.* 413–416 (2011).
9. Ielmini, D. Modeling the universal set/reset characteristics of bipolar RRAM by field- and temperature-driven filament growth. *IEEE Trans. Electron Devices* **58**, 4309–4317 (2011).
10. Menzel, S. *et al.* Origin of the ultra-nonlinear switching kinetics in oxide-based resistive switches. *Adv. Funct. Mater.* **21**, 4487–4492 (2011).
11. Kwon, D.-H. *et al.* Atomic structure of conducting nanofilaments in TiO$_2$ resistive switching memory. *Nat. Nanotechnol.* **5**, 148–153 (2010).
12. Strachan, J. P. *et al.* Direct identification of the conducting channels in a functioning memristive device. *Adv. Mater.* **22**, 3573–3577 (2010).
13. Yu, S., Wu, Y. & Wong, H.-S. P. Investigating the switching dynamics and multilevel capability of bipolar metal oxide resistive switching memory. *Appl. Phys. Lett.* **98**, 103514 (2011).
14. Huang, P. *et al.* A physical-based analytic model of RRAM operation for circuit simulation. *IEDM Tech. Dig.* 606–608 (2012).
15. Lee, M.-J. *et al.* A fast, high-endurance and scalable non-volatile memory device made from asymmetric Ta$_2$O$_{5−x}$/TaO$_{2−x}$ bilayer structures. *Nat. Mater.* **10**, 625–630 (2011).
16. Hur, J.-H. *et al.* Modeling for multilevel switching in oxide-based bipolar resistive memory. *Nanotechnology* **23**, 225702 (2012).
17. Larentis, S., Cagli, C., Nardi, F. & Ielmini, D. Filament diffusion model for simulating reset and retention processes in RRAM. *Proc. Microelectron. Eng.* 1119–1123 (2011).
18. Mott, M. F. & Gurney, R. W. Electronic Processes in Ionic Crystals. *Dover: U. K.* (1948).
19. Russo, U., Kalamanathan, D., Ielmini, D., Lacaita, A. L. & Kozicki, M. Study of multilevel programming in programmable metallization cell (PMC) memory. *IEEE Trans. Electron Devices* **56**, 1040–1047 (2009).
20. Yu, S. & Wong, H.-S. P. Compact modeling of conducting-bridge random-access memory (CBRAM). *IEEE Trans. Electron Devices* **58**, 1352–1360 (2011).
21. Ielmini, D., Nardi, F. & Cagli, C. Physical models of size-dependent nanofilament formation and rupture in NiO resistive switching memories. *Nanotechnology* **22**, 254022 (2011).
22. Henager, C. H. & Pawlewicz, W. T. Thermal conductivities of thin, sputtered optical films. *Applied Optics* **32**, 91–101 (1993).
23. Yun, J.-B. *et al.* Random and localized resistive switching observation in Pt/NiO/Pt. *Phys. Stat. Sol. (RRL)* **1**, 280–282 (2007).
24. Kim, K. M. & Hwang, C. S. The conical shape filament growth model in unipolar resistance switching of TiO$_2$ thin film. *Appl. Phys. Lett.* **94**, 122109 (2009).
25. Bersuker, G. *et al.* Metal oxide RRAM switching mechanism based on conductive filament microscopic properties. *IEDM Tech. Dig.* 456–459 (2010).

Author contributions

S.K., S.-J.K., Y.-B.K., C.J.K. conceived and designed the experiment. K.M.K., S.R.L., E.C. prepared the samples and S.K. conducted the experiment and contributed to writing the manuscript. U.-I.C., I.-K.Y. supervised the research. All authors discussed the results.

Additional information